19. Gaston, A. J. The ecology and behaviour of the long-tailed tit. *Ibis (Lond.)* **115,** 330–351 (1973).

20. Sharp, S. P. *Kin Recognition in the Cooperative Breeding System of the Long-tailed Tit,* Aegithalos caudatus. Thesis, Univ. Sheffield (2003).

21. Sharp, S. P. & Hatchwell, B. J. Individuality in the contact calls of cooperatively breeding long-tailed tits. *Behaviour* (in the press).

22. Brittan-Powell, E. F., Dooling, R. J. & Farabaugh, S. M. Vocal development in budgerigars (*Melopsittacus undulatus*): contact calls. *J. Comp. Psychol.* **111,** 226–241 (1997).

23. Price, J. J. Family- and sex-specific vocal traditions in a cooperatively breeding songbird. *Proc. R. Soc. Lond. B* **265,** 497–502 (1998).

24. Hatchwell, B. J., Ross, D. J., Chaline, N., Fowlie, M. K. & Burke, T. Parentage in the cooperative breeding system of long-tailed tits, *Aegithalos caudatus. Anim. Behav.* **64,** 55–63 (2002).

25. Hatchwell, B. J., Anderson, C., Ross, D. J., Fowlie, M. K. & Blackwell, P. G. Social organization of cooperatively breeding long-tailed tits: kinship and spatial dynamics. *J. Anim. Ecol.* **70,** 820–830 (2001).

26. Komdeur, J., Richardson, D. S. & Burke, T. Experimental evidence that kin discrimination in the Seychelles warbler is based on association and not on genetic relatedness. *Proc. R. Soc. Lond. B* **271,** 963–969 (2004).

27. MacColl, A. D. C. & Hatchwell, B. J. Sharing of caring: nestling provisioning behaviour of long-tailed tit, *Aegithalos caudatus,* parents and helpers. *Anim. Behav.* **66,** 955–964 (2003).

28. Siegel, S. & Castellan, N. J. *Nonparametric Statistics for the Behavioral Sciences* (McGraw-Hill, Boston, 1988).

A synthetic multicellular system for programmed pattern formation

Subhayu Basu[1], **Yoram Gerchman**[1], **Cynthia H. Collins**[3], **Frances H. Arnold**[3] **& Ron Weiss**[1,2]

[1]*Department of Electrical Engineering and* [2]*Department of Molecular Biology, Princeton University, Princeton, New Jersey 08544, USA*
[3]*Division of Chemistry and Chemical Engineering, California Institute of Technology 210-41, Pasadena, California 91125, USA*

Pattern formation is a hallmark of coordinated cell behaviour in both single and multicellular organisms[1–3]. It typically involves cell–cell communication and intracellular signal processing. Here we show a synthetic multicellular system in which genetically engineered 'receiver' cells are programmed to form ring-like patterns of differentiation based on chemical gradients of an acyl-homoserine lactone (AHL) signal that is synthesized by 'sender' cells. In receiver cells, 'band-detect' gene networks respond to user-defined ranges of AHL concentrations. By fusing different fluorescent proteins as outputs of network variants, an initially undifferentiated 'lawn' of receivers is engineered to form a bullseye pattern around a sender colony. Other patterns, such as ellipses and clovers, are achieved by placing senders in different configurations. Experimental and theoretical analyses reveal which kinetic parameters most significantly affect ring development over time. Construction and study of such synthetic multicellular systems can improve our quantitative understanding of naturally occurring developmental processes and may foster applications in tissue engineering, biomaterial fabrication and biosensing.

Figure 1a depicts the design of the synthetic bacterial multicellular system, showing how only receivers at intermediate distances from senders express the output protein. Cell–cell communication from the senders is initiated by expression of the LuxI enzyme[4,5] (Fig. 1b). LuxI catalyses the synthesis of AHL, which diffuses through the cell membrane and forms a chemical gradient around the senders. AHL diffuses into nearby receiver cells and is bound by LuxR, an AHL-dependent transcriptional regulator, which activates the expression of lambda repressor (CI) and Lac repressor (LacI$_{M1}$, a product of a codon-modified *lacI*). Receiver cells in close proximity to the senders receive high concentrations of AHL, resulting in high cytoplasmic levels of CI and LacI$_{M1}$ and repression of the green fluorescent protein (GFP). Receivers that are far from the senders have low AHL concentrations, and accordingly LacI$_{M1}$ and CI are expressed only at basal levels. This enables the expression of a wild-type LacI, again resulting in GFP repression. At intermediate distances from the senders, intermediate AHL concentrations result in moderate levels of CI and LacI$_{M1}$. However, because the repression efficiency of CI is significantly higher than that of LacI$_{M1}$, CI effectively shuts off LacI expression while the LacI$_{M1}$ concentration is below the threshold required to repress GFP production. This difference between the CI and LacI$_{M1}$ repression efficiencies, in combination with a feed-forward loop[6] that begins with LuxR and culminates in GFP, affords the circuit the desired non-monotonic response to AHL dosages.

Guided by a mathematical model, the band-detect behaviour was engineered by combining a high-detect component (pHD plasmids; Fig. 1c) with a low-detect component (pLD plasmid; Fig. 1d) as described below. The high-detect component determines the AHL threshold above which GFP expression is muted. We engineered three high-detect strains (HD1, HD2 and HD3), each harbouring a variant of the high-detect plasmid (pHD{x}; Fig. 1c). The HD1 strain contains a hypersensitive LuxR mutant[7], HD2 incorporates the wild-type LuxR, and HD3 cells express LuxR from a reduced-copy-number plasmid. In agreement with model predictions (Fig. 2a), the liquid-phase dosage responses of these three HD strains showed inverse correlations to AHL concentrations with different sensitivities (Fig. 2b). The low-detect component determines the lowest concentration of AHL that elicits GFP response. By combining the low-detect plasmid with each of the high-detect plasmid variants, we obtained three different band-detect strains named BD1, BD2 and BD3 accordingly. The BD strains showed a non-monotonic response to AHL with different thresholds (Fig. 2d), which correlated well with model predictions (Fig. 2c). Taken together, the responses of the three variants cover a wide range of biologically relevant AHL concentrations. Further analysis showing the effects of LacI and CI repression efficiencies on band-detect behaviour is included in the Supplementary Information.

Spatiotemporal simulations of a band-detect system predicted that by placing sender cells capable of AHL synthesis next to receiver cells, the above network could direct pattern formation on solid media. The model showed that given the appropriate kinetics for circuit elements, a distinct ring pattern would form in an initially undifferentiated 'lawn' of receiver cells around a group of sender cells (see Methods). Furthermore, a bullseye pattern could be achieved by mixing band-detect network variants such as BD1, BD2 and BD3. We tested these model predictions by plating on a Petri dish a mixture of BD3 cells and BD2-Red cells (similar to BD2 with *dsRed-Express* replacing *gfp*). A disk containing sender cells was placed in the middle of the dish (Fig. 3a), and the dish was incubated overnight. Microscope fluorescence images were subsequently captured. As seen in Fig. 3b, BD3 cells formed a green fluorescent ring near the senders, whereas BD2-Red cells formed a red fluorescent ring located further from the senders, creating a bullseye pattern. Similarly, when BD1 and BD2-Red cells were mixed and plated with a sender disk, an outer green fluorescent ring appeared around the red fluorescent ring (Fig. 3c). Although the relative positions of BD1, BD2 and BD3 cells were consistent in the two experiments, the diameters of the two BD2-Red rings were somewhat different (30 mm versus 22 mm). This can be attributed to variations in the AHL gradients due to differences in the growth rates and population

densities of senders and receivers, as well as subtle environmental differences between experiments such as nutrient conditions and agar densities.

Understanding the dynamic behaviour of the system is crucial in predicting pattern formation. To study system dynamics, we measured the ring formation activity of BD2 cells over the course of 36 h. Fluorescence was recorded every 90 min for a 30 mm × 4 mm rectangular region protruding from the sender disk (Fig. 4a). For the first 15 h no fluorescence was observed, and then low levels of fluorescence emerged about 10 mm from the senders. Fluorescence values then increased significantly between 5 and 18 mm from the senders; these values stabilized after about 32 h, reaching a steady-state maximum at 10 mm (Fig. 4a). Over the duration of the experiment there was no observable shift in the position of high fluorescence.
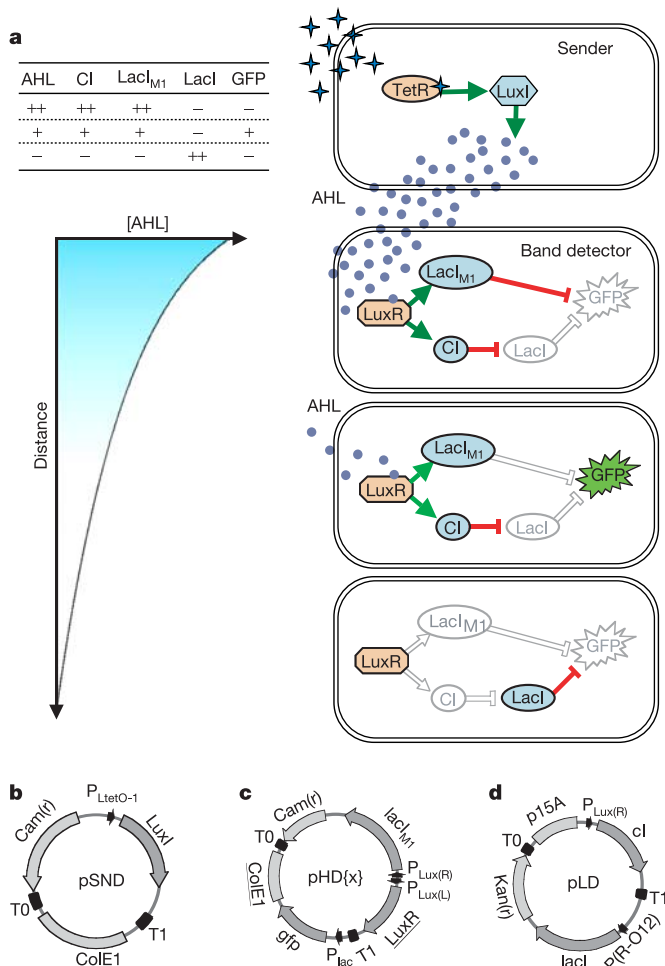
To gain a better understanding of circuit factors influencing ring formation dynamics, we performed and analysed 100 spatiotemporal simulations with different sets of kinetic rate constants. In all simulations, the senders' AHL synthesis rates were modified to ensure that fluorescence rings always formed at the same distance from the senders (as described in Methods). Figure 4b, c shows two simulations of the band-detect network with two different sets of kinetic rates. In comparison, the region of high fluorescence in Fig. 4c appears more quickly and stabilizes earlier, and its position shifts over a wider distance than in Fig. 4b. Statistical analysis of the entire set of simulations revealed that the rate constant for LacI decay had the strongest correlation with fluorescence response times and positional shift. These correlations are shown in Fig. 4d, e, where each point captures the response times (shift begin, shift end) and positional shift of one of the above simulations. The shift begin value is the time at which high fluorescence first appears, shift end is the time it takes the ring to form at the final position, and positional shift is the distance over which the ring expands until it stabilizes. The trend lines, computed as described in Methods, show a significant correlation between the rate constant for LacI decay and shift begin (Fig. 4d; $R^2 = 0.91$, $P < 0.0001$), shift end (Fig. 4d; $R^2 = 0.71$, $P < 0.0001$) and positional shift (Fig. 4e; $R^2 = 0.76$, $P < 0.0001$).

The stability of LacI affects how closely GFP expression in the receivers reports on the establishment of the AHL gradient from the senders. Before GFP expression can begin, AHL has to activate the production of CI, and LacI levels must subsequently decline. Fast rate constants for LacI decay will cause fluorescence to emerge quickly at a site far from the steady-state position, and then shift as the AHL gradient builds over time until it stabilizes. Circuits with intermediate LacI stability (decay rates between 0.02 min^{-1} and
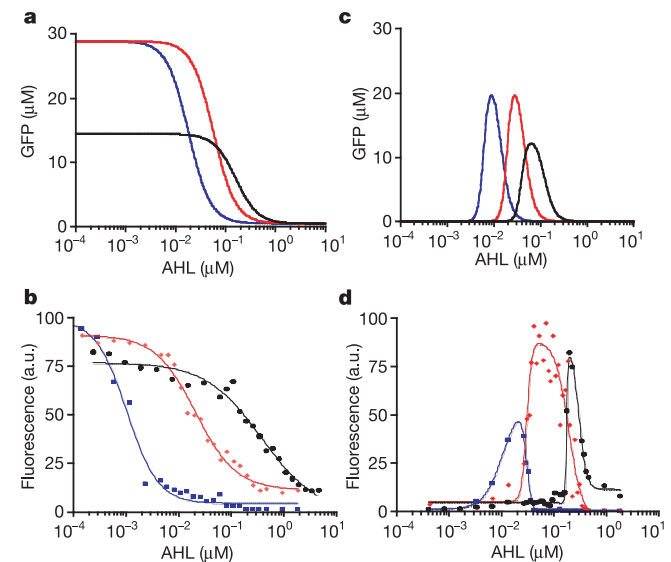

Figure 1 The band-detect multicellular system programs *E. coli* receiver cells to fluoresce only at intermediate distances from sender cells. **a**, Circuit operation for a sender and three receivers exposed to high, medium or low AHL concentrations, showing the correlation of the various AHL and protein levels (top left), approximation of the AHL gradient as a function of the distance from the senders (bottom left) and the relevant protein activities in cells at different distances from the senders as mediated through transcriptional regulation (right; orange, constitutively expressed response proteins; blue/green, expression of regulated proteins; green and red arrows, transcriptional induction and repression respectively). High levels of LacI or LacI$_{M1}$ (indicated by ++) are required to repress GFP. **b**, Plasmid map for senders. **c**, **d**, The high-detect (**c**) and low-detect (**d**) plasmids that implement the band-detect operation. Three versions of the high-detect plasmid with different sensitivities to AHL were constructed (regions of mutation are underlined: pHD1, LuxR; pHD2, wild-type; pHD3, ColE1).

Figure 2 Simulated and experimental liquid-phase behaviour of high-detect and band-detect networks. **a**, **b**, Simulations (**a**) and experimental results (**b**) of the AHL dosage response for three high-detect network variants with wild-type LuxR (HD2, red), a hypersensitive LuxR (HD1, blue) and a reduced-copy-number plasmid (HD3, black). For the curve fits, the 95% confidence intervals have minimum/maximum values of 2.03/6.58, 2.47/4.14 and 2.78/5.12 for HD1, HD2 and HD3, respectively. **c**, **d**, Band detect simulations (**c**) and experimental results (**d**) of three networks consisting of the high-detect variants from above and the same low-detect component (BD1, blue), BD2 (red) and BD3 (black) contain the high-detect components from HD1, HD2 and HD3, respectively. For the curve fits, the 95% confidence intervals have minimum/maximum values of 0.48/4.43, 7.36/18.55 and 1.1/8.23 for BD1, BD2 and BD3, respectively. a.u., arbitrary units.
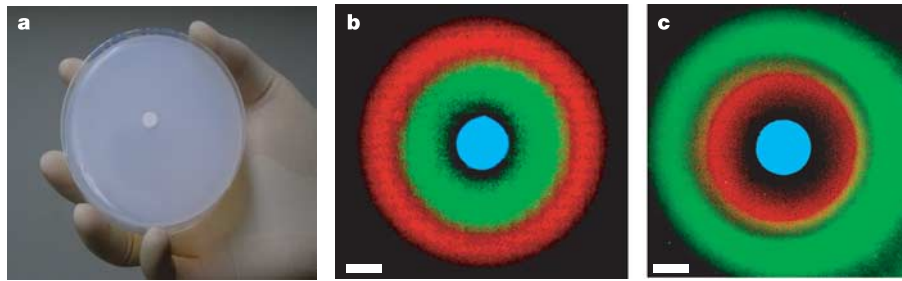
Figure 3 Experimental solid-phase behaviour of band-detect networks. **a**, Picture of the Petri dish used in the BD2-Red/BD3 experiment showing the sender disk in the middle. **b**, Bullseye pattern as captured with a fluorescence microscope after incubation overnight with senders in the middle of an initially undifferentiated 'lawn' of BD2-Red and BD3 cells. Surface maps depicting red and green fluorescence intensities are included in Supplementary Information. The senders in the middle are expressing CFP. **c**, Another bullseye pattern, this time with a mixture of BD1 and BD2-Red cells. Scale bar, 5 mm.

$0.04\,\text{min}^{-1}$) form rings at the final position only, but do not incur a significant time delay. Rate constants for LacI decay of less than $0.02\,\text{min}^{-1}$ also show no positional shift but result in a very slow emergence of fluorescence long after the AHL gradient has stabilized. The effect of LacI stability is also demonstrated by comparing Fig. 4b with Fig. 4c, where an important difference between these two kinetic parameter sets is a shorter half-life for LacI in Fig. 4b. We therefore postulated that the relatively long half-life of LacI (in our experimental system LacI degradation is due mainly to dilution by cell growth) accounts for the similarity
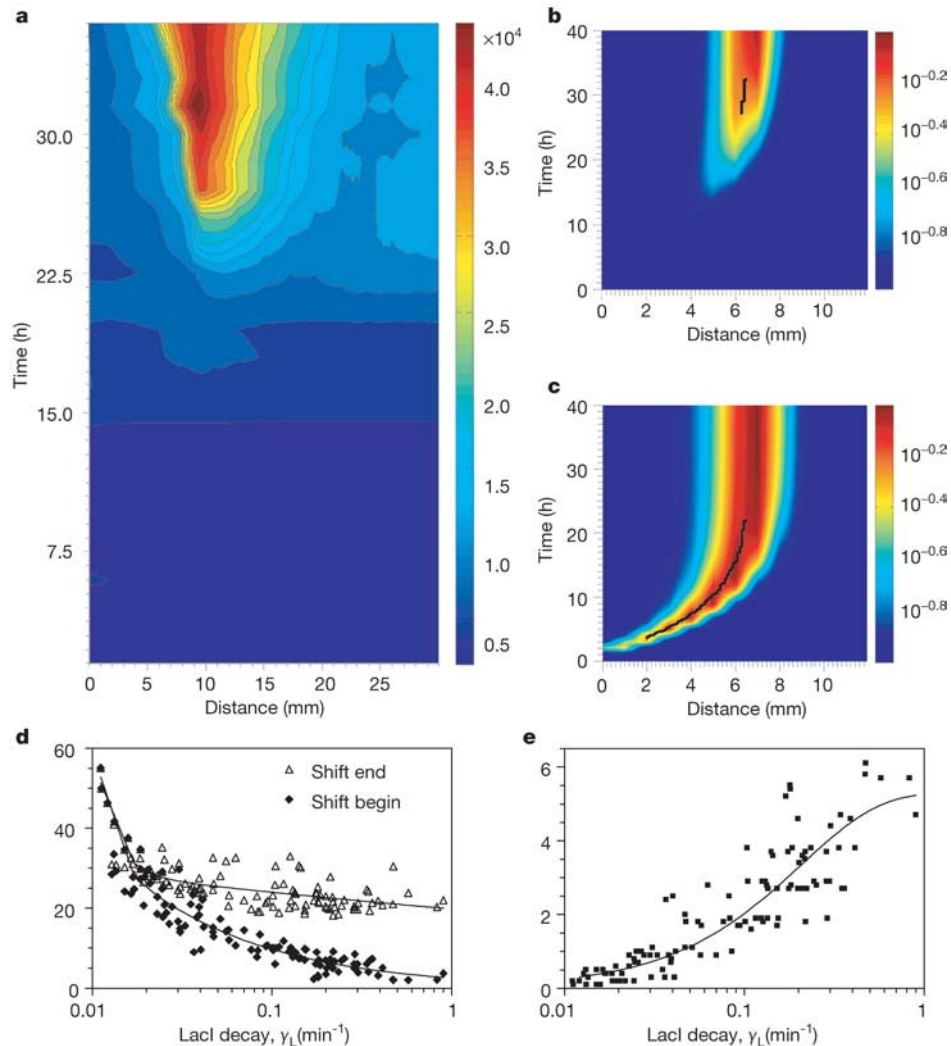

Figure 4 Ring formation dynamics. **a**, Experimental results showing the time-evolution of fluorescence for band-detect cells as a function of the distance from the senders. **b**, **c**, Spatiotemporal simulations of two shifts with different sets of kinetic parameters that form the ring at the same distance. Maximal levels of fluorescence are indicated by red, while the black lines represent the spatiotemporal shift of the ring. The shift associated with a fast decaying LacI (**c**) is larger than the shift resulting from a stable LacI (**b**). **d**, Regression analysis correlating the fluorescence response times with rate constants for LacI decay. Open triangles, shift end; filled diamonds, shift begin. **e**, Regression analysis correlating positional shift with rate constants for LacI decay.
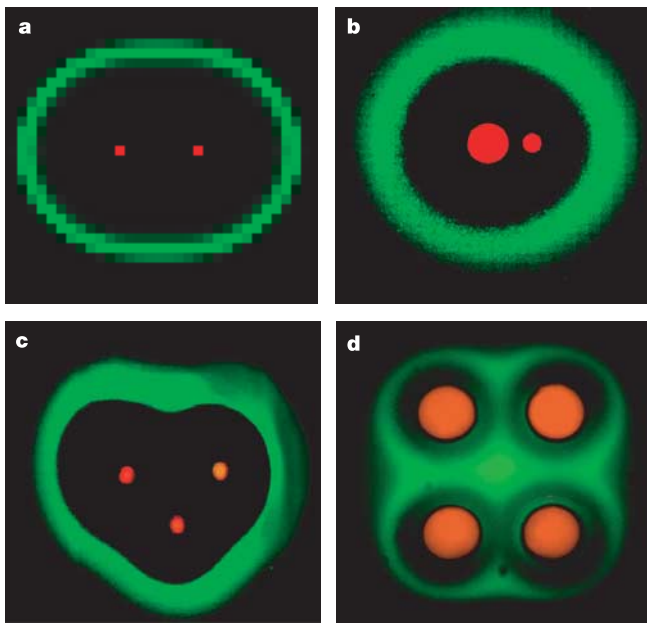
Figure 5 Formation of various patterns. **a**, Simulation of band-detect behaviour on solid media with two senders that results in the formation of an ellipse. **b–d**, Experimental results showing various GFP patterns formed based on the placement and initial concentrations of sender cells expressing DsRed-Express: **b**, ellipse, two sender disks; **c**, heart, three sender disks; and **d**, clover, four sender disks.

between the experimental observations in Fig. 4a and the results of the simulation in Fig. 4b. For the other rate constants, CI repression efficiency showed a weak correlation with the positional shift ($R^2 = 0.05$, $P = 0.0191$), whereas the rest of the rate constants from equations (1)–(4) did not show any correlation ($R^2 < 0.001$, $P > 0.75$).

The dynamics and final pattern of differentiation depend not only on the receiver network but also on the spatial arrangement of senders. We directed this multicellular system to form more elaborate patterns by placing multiple sender disks in different configurations. By changing initial conditions (for example the number of, distance between, and density of sender cells) one can create different AHL gradients and hence direct the formation of different intricate patterns (Fig. 5). In the future, more complex multicellular patterns with improved properties will be achieved by integrating bi-directional communication.

Natural systems are often a good source of inspiration for the forward design of synthetic circuits. For example, in *Drosophila melanogaster* blastoderm segmentation, inhibitory feedback loops between communicating elements help to demarcate domain boundaries[8]. By incorporating similar intercellular feedback loops, future artificial multicellular systems could create patterns with sharper edges. However, the feedback loops found in *D. melanogaster* are also responsible for 'domain shifts'[9]. Although some patterns of gene expression are spatiotemporally stable (Kruppel), others shift over time (giant, knirps)[9]. Such a shift might be undesirable and even destructive in certain synthetic systems, for example tissue-engineering applications. Nevertheless, as shown by the statistical analysis above, this problem can be overcome by careful engineering of system components. The construction and analysis of artificial systems such as the band-detect network can also help to improve our understanding of biological design principles. These domain shifts in *D. melanogaster* are accompanied by a sharpening of the gene expression zones and probably represent an important fine tuning of the location and size of these zones. We suggest that such natural patterning systems have evolved finely

tuned protein decay rates that allow them to function with the precision required during development. It will be interesting to see whether the shift/no-shift property is indeed controlled by careful matching between intracellular protein decay dynamics and extra-cellular diffusion processes.

The work described here shows the design and construction of an artificial multicellular system capable of programmed pattern formation. We have shown how a community of cells can sense a chemical gradient to form three distinct regions. The system consists of simple parts that are arranged in different configurations to elicit the desired patterns. Theoretical and experimental analyses of system behaviour are facilitated by the fact that the parts are well characterized and can be fine-tuned. the integration of such systems into higher-level organisms and with different cell functions will have practical applications in three-dimensional tissue engineering, biosensing, and biomaterial fabrication. We see the construction of this and similar systems as a step towards creating artificial differentiation patterns on demand and contributing to a better understanding of natural developmental processes. □

Methods

Plasmids

Plasmids and their properties are listed in Supplementary Table S1. The sender plasmid pSND encodes LuxI controlled by $P_{LTet-O1}$ promoter[10]. Band-detect cells contain two plasmids, low-detect plasmid (pLD) and high-detect plasmid (pHD{x}). pLD encodes a destabilized λ repressor[11] (CI) controlled by $P_{lux(R)}$ (ref. 12) and a *lac* repressor (LacI) controlled by $λ_{P(R-O12)}$ (ref. 13), and was constructed from pLTSUB-202 (ref. 14) and pRCV-3 (ref. 10). pHD2 was made from pRCV-102 (ref. 15) and pINV-4 (ref. 15), and contains LuxR, LacI$_{M1}$ and GFP under the control of $P_{lux(L)}$, $P_{lux(R)}$ and P_{lac}, respectively. *lacI*$_{M1}$ is a codon-modified *lacI* designed to reduce the likelihood of recombination with the wild-type *lacI* on the pLD plasmid. pHD1 is a variant of pHD2 with a hypersensitive variant of LuxR, LuxR-G2F (ref. 7). pHD3 is a variant of pHD1 with an AT → TA mutation in ColE1 *ori* positions 222–223 that approximately halves the plasmid copy number (data not shown). pHD2-Red was made from pHD2 by replacing GFP with DsRed-Express. All proteins except LuxR are preceded by a strong synthetic ribosome-binding site, RBSII[13], whereas LuxR is preceded by its native RBS. CI and GFP are destabilized with an 11-amino-acid ssrA LVA tag[16].

Data acquisition and analysis

Escherichia coli strain DH5α (λ −, recA1 −) (CGSC strain 7855) was used for all experiments. Cells transformed with the appropriate plasmids were grown at 37 °C in M9 minimal medium (0.2% casamino acids, 200 μM thiamine, 100 μM CaCl$_2$), with antibiotics (50 μg ml^{-1} kanamycin, 25 μg ml^{-1} chloramphenicol) until exponential phase (optical density at 600 nm (OD 600) = 0.3). For the liquid-phase experiments, expression was induced by the addition of 3-oxohexanoyl homoserine-lactone (3OC$_6$HSL; Sigma-Aldrich). Receiver cultures were analysed by fluorescence-activated cell sorting (FACS) with a Beckman Coulter Altra (488-nm argon excitation laser, 515–545-nm emission filter) and measurements were calibrated using Spherotech SPHERO Rainbow Calibration Particles (RCP-30-5A). Data points represent median FACS values. Figure 2c curves were fitted to a sigmoidal function,

$$y = y_0 + \left(\frac{\alpha}{1 + (AHL/\beta)^n} \right)$$

and Fig. 2d curves were fitted to a bell-shaped dose–response function,

$$y = \delta + \left(\frac{(\alpha_1 - \delta)}{1 + (AHL/\beta_1)^{n_1}} \right) + \left(\frac{(\alpha_2 - \delta)}{1 + (AHL/\beta_2)^{-n_2}} \right)$$

using GraphPad PRISM software. For the solid-phase experiment, time-lapse microscopy was conducted on a Zeiss Axiovert 200M microscope equipped with a 1344-pixel × 1024-pixel cooled ORCA-ER charge-coupled device camera (Hamamatsu). Separate cultures of band-detect cells were grown to an OD 600 of 0.3, washed with M9 salts, diluted into 2 ml of 0.7% agarose to achieve an OD 600 of 0.15, and spread evenly on top of an M9 1.5% agarose plate. Senders were grown in a similar manner and then concentrated 50-fold. Senders (20 μl) were pipetted onto a Whatman 3 paper disk and placed in the centre of the plate. Plates were incubated at 37 °C. Brightfield and fluorescence images were captured with a 2.5× brightfield objective. False colouring was performed by capturing images with filters optimized for the different fluorescent proteins and then superimposing the images with the appropriate colours and assembling them into larger mosaics with custom software (CFP filters, 436/20 excitation and 470/30 emission; GFP, 470/40 and 525/50; DsRedExpress, 565/30 and 620/60).

Model

A simple five-species model was used to model both the single-cell band-detect response to AHL and the spatiotemporal behaviour of a multicellular sender–receiver system (using the modelling tool described previously[14]). The models were based on ordinary differential equations with Hill functions that captured the activation and repression of protein synthesis. The intracellular species included GFP (G), LacI (L), CI (C), LuxR/AHL

complex (R), AHL (A) and a fixed concentration of LuxR. The following equations were used:

$$\frac{dG}{dt} = \frac{\alpha_G}{1 + (L/\beta_L)^{\eta 1}} - \gamma_G G \qquad (1)$$

$$\frac{dL}{dt} = \frac{\alpha_{L1}}{1 + (C/\beta_C)^{\eta 2}} + \frac{\alpha_{L2} \cdot R^{\eta 3}}{(\theta_R)^{\eta 3} + R^{\eta 3}} - \gamma_L L \qquad (2)$$

$$\frac{dC}{dt} = \frac{\alpha_C R^{\eta 3}}{(\theta_R)^{\eta 3} + R^{\eta 3}} - \gamma_C C \qquad (3)$$

$$\frac{dR}{dt} = \rho_R [LuxR]^2 A^2 - \gamma_R R \qquad (4)$$

$$\frac{dA_{x,y,z}}{dt} = \xi(A_{x-1,y,z} + A_{x+1,y,z} + A_{x,y-1,z} + A_{x,y+1,z} + A_{x,y,z-1} + A_{x,y,z+1} - 6A_{x,y,z})$$
$$- \gamma_A \qquad (5)$$

The following parameters approximate the behaviour of BD2: protein synthesis rates (α_G, 2 μM min^{-1}; α_{L1}, 1 μM min^{-1}; α_{L2}, 1 μM min^{-1}; α_C, 1 μM min^{-1}), repression coefficients (β_L, 0.8 μM; β_C, 0.008 μM), protein decay (γ_C and γ_G, 0.0692 min^{-1}; γ_L and γ_R, 0.0231 min^{-1}), LuxR/AHL activation coefficient (θ_R, 0.01 μM), transcription factor cooperativity/multimerization (η_1, 2; η_2, 2; η_3, 1), LuxR/AHL dimerization (ρ_R, 0.5 μM^{-3} min^{-1}), AHL intercellular diffusion (ξ, 0.001 mm^2 min^{-1}) and AHL decay (γ_A, 0.01 min^{-1}). LuxR concentration was set at 0.5 μM. LuxR and AHL first bind to form a complex, and this complex then dimerizes to form an active transcription factor[17]; hence the quadratic terms in equation (4). The degradation rate of AHL (γ_A), which determines the steepness of the chemical gradient, is affected by pH (ref. 18). The liquid-phase simulations did not include equation (5). Further, to simulate the high-detect component in the liquid phase, equation (3) and CI repression in equation (2) were also not used. For the HD1 and BD1 liquid simulations, ρ_R was increased tenfold from above, whereas for the HD3 and BD3 simulations the values of α_G, α_{L2} and [LuxR] were halved.

For the statistical analysis of the shift, we first generated 2,000 sets of random kinetic parameters, in which the values for each parameter were uniformly distributed around those used above. Among these sets, about 30% yielded band-detect behaviour with a gain greater than three and fluorescence values above a predetermined threshold. For the first 100 sets we computed the AHL synthesis rate resulting in ring formation centred at 7 mm from the senders. Using each parameter set, we simulated system behaviour until GFP at all positions stabilized, and computed the shift as follows. The beginning of a shift is defined as the spatiotemporal coordinate $\langle$position$_{start}$, time$_{start}\rangle$ that meets the following criteria: it is in the middle of the ring for that particular time, it is closest to the origin, and its fluorescence is greater than 50% of maximum overall steady-state fluorescence. The end of a shift is defined as the spatiotemporal coordinate $\langle$position$_{steady}$, time$_{steady}\rangle$ that meets the same criteria as above and is located at the final steady-state position of the ring. The positional shift is then the difference between position$_{steady}$ and position$_{start}$.

In Fig. 4b, c the following values were changed from above (β_L, 543/230 nM; β_C, 19/69 nM; γ_C, 0.116/0.496 min^{-1}; γ_G, 0.404/0.366 min^{-1}; γ_L, 0.018/0.902 min^{-1}; γ_R, 0.036/0.050 min^{-1}; θ_R, 0.249/0.063 μM; ρ_R, 2.102/3.374 μM^{-3} min^{-1}). GraphPad PRISM software was used to perform a regression analysis correlating each of the rate constants with the corresponding shift values. The response times were correlated by using power-series equations and the positional shift was correlated with a sigmoidal fit.

1. Golden, J. & Yoon, H. Heterocyst formation in *anabaena*. *Curr. Opin. Microbiol.* **1,** 623–629 (1998).
2. Scherrer, R. & Shull, V. Structure, partial elemental composition, and size of *Thiopedia rosea* cells and platelets. *Can. J. Microbiol.* **32,** 607–610 (1986).
3. Ben-Jacob, E. *et al.* Cooperative formation of chiral patterns during growth of bacterial colonies. *Phys. Rev. Lett.* **75,** 2899–2902 (1995).
4. Fuqua, W. C., Winans, S. & Greenberg, E. P. Quorum sensing in bacteria: The luxR-luxI family of cell density-responsive transcriptional regulators. *J. Bacteriol.* **1760,** 269–275 (1994).
5. Bassler, B. L. How bacteria talk to each other: regulation of gene expression by quorum sensing. *Curr. Opin. Microbiol.* **2,** 582–587 (1999).
6. Milo, R. *et al.* Network motifs: simple building blocks of complex networks. *Science* **298,** 824–827 (2002).
7. Collins, C. H., Arnold, F. H. & Leadbetter, J. R. Directed evolution of *Vibrio fischeri* LuxR for increased sensitivity to a broad spectrum of acyl-homoserine lactones. *Mol. Microbiol.* **55,** 712–723 (2005).
8. Jaeger, J. *et al.* Dynamical analysis of regulatory interactions in the gap gene system of *Drosophila melanogaster*. *Genetics* **167,** 1721–1737 (2004).
9. Jaeger, J. *et al.* Dynamic control of positional information in the early *Drosophila* embryo. *Nature* **430,** 368–371 (2004).
10. Weiss, R. & Knight, T. F. Jr in *DNA6: Sixth International Workshop on DNA-Based Computers, DNA2000* (eds Condon, A. & Rozenberg, G.) 1–16 (Springer, Leiden, The Netherlands, 2000).
11. Ptashne, M. *A Genetic Switch: Phage Lambda and Higher Organisms*, 2nd edn (Cell Press and Blackwell Scientific Publications, Cambridge, Massachusetts, 1986).
12. Egland, K. A. & Greenberg, E. P. Quorum sensing in *Vibrio fischeri*: elements of the *luxI* promoter. *Mol. Microbiol.* **31,** 1197–1204 (1999).
13. Weiss, R. & Basu, S. in *NSC-1: The First Workshop on Non Silicon Computing* ⟨http://www-2.cs.cmu.edu/~phoenix/nsc1/paper/3-2.pdf⟩ (2002).
14. Basu, S., Mehreja, R., Thiberge, S., Chen, M. & Weiss, R. Spatiotemporal control of gene expression with pulse-generating networks. *Proc. Natl Acad. Sci. USA* **101,** 6355–6360 (2004).
15. Weiss, R. *Cellular Computation and Communication Using Engineered Genetic Regulatory Networks.* Ph.D. thesis, Massachusetts Inst. Technology (2001).
16. Andersen, J. B. *et al.* New unstable variants of green fluorescent protein for studies of transient gene expression in bacteria. *Appl. Environ. Microbiol.* **64,** 2240–2246 (1998).
17. Choi, S. H. & Greenberg, E. P. Genetic evidence for multimerization of LuxR, the transcriptional activator of *Vibrio fischeri* luminescence. *Mol. Mar. Biol. Biotechnol.* **6,** 408–413 (1992).
18. Yates, E. A. *et al.* N-acylhomoserine lactones undergo lactonolysis in a pH-, temperature-, and acyl chain length-dependent manner during growth of *Yersinia pseudotuberculosis* and *Pseudomonas aeruginosa. Infect. Immun.* **70,** 5635–5646 (2002).

....

Dynamics of *Drosophila* embryonic patterning network perturbed in space and time using microfluidics

Elena M. Lucchetta[1], **Ji Hwan Lee**[1], **Lydia A. Fu**[1], **Nipam H. Patel**[2] **& Rustem F. Ismagilov**[1]

[1]*Department of Chemistry, University of Chicago, Chicago, Illinois 60637, USA*
[2]*Department of Integrative Biology, Molecular and Cell Biology, and Howard Hughes Medical Institute, University of California Berkeley, Berkeley, California 94720-3140, USA*

....

Biochemical networks are perturbed both by fluctuations in environmental conditions and genetic variation. These perturbations must be compensated for, especially when they occur during embryonic pattern formation. Complex chemical reaction networks displaying spatiotemporal dynamics have been controlled and understood by perturbing their environment in space and time[1–3]. Here, we apply this approach using microfluidics to investigate the robust network in *Drosophila melanogaster* that compensates for variation in the Bicoid morphogen gradient. We show that the compensation system can counteract the effects of extremely unnatural environmental conditions—a temperature step—in which the anterior and posterior halves of the embryo are developing at different temperatures and thus at different rates. Embryonic patterning was normal under this condition, suggesting that a simple reciprocal gradient system is not the mechanism of compensation. Time-specific reversals of the temperature step narrowed down the critical period for compensation to between 65 and 100 min after onset of embryonic development. The microfluidic technology used here may prove useful to future studies, as it allows spatial and temporal regulation of embryonic development.

Although rates of production and degradation of morphogens are affected by genetic and environmental variations, the mechanisms of embryo patterning have evolved to compensate for these variations. In *Drosophila melanogaster*, morphogens such as Bicoid protein act early on in the genetic hierarchy that patterns the *Drosophila* embryo along the antero-posterior axis. Altering the copy number of *bicoid* genes shifts the Bicoid expression profile and results in shifting of the expression pattern of a direct downstream target gene, *hunchback*, and subsequent expression of pair-rule and segment polarity genes[4]. The expression profile of the maternal Bicoid protein gradient, however, varies measurably between individual wild-type embryos, and is particularly affected by variations